Coupling between shallow and deep fault populations governs along-strike variations in fault reactivation and structural inheritance, the Laminaria High, NW Shelf of Australia

Thomas B. Phillips*, Ken McCaffrey, Luke Magarinos

*Thomas.b.phillips@durham.ac.uk

Department of Earth Science, Durham University, Science Labs,

Abstract

When extension events are greatly separated in time, older faults may be buried and stratigraphically separated from newly developing faults at shallower depths. During rifting, the buried structures may reactivate and propagate upwards to be expressed within the shallow system. The degree of linkage between structural levels determines the influence that the deeper structures can exert over the geometry and evolution of the incipient fault system. In this study we use 3D seismic reflection data to examine how a deep fault population across the Laminaria High, NW shelf of Australia influences the development of a younger system at shallow depths. These fault populations are non-collinear and decoupled across a mechanically weak interval. The majority of shallow faults are not linked to those at depth, however the reactivation and upwards propagation of deeper faults produces anomalously oriented structures at shallow depths, hard-linked to the deeper structures. One fault in particular shows along-strike variability along its length, with the deep segment reactivated and present at shallow depths in the west. To the east, the shallow and deep fault segments become decoupled across mechanically weak interval, although some soft-linkage and strain transfer still occurs. We suggest that this switch in the degree of coupling along the fault is due to the geometry of the deeper structure, with the transition corresponding to a prominent relay ramp. We show how the geometry of a deeper fault may affect its propensity to reactivate during subsequent extensional events, ultimately affecting the degree of structural inheritance that is expressed within younger, shallower fault populations.

1 Introduction

During extension, faults formed during earlier rift phases exert variable degrees of influence over the geometric and kinematic evolution of the incipient fault population (Henstra et al., 2019; Henza et al., 2011; Reeve et al., 2015; Whipp et al., 2014). Younger faults may completely or partially reactivate older structures (e.g. Duffy et al., 2015; Nixon et al., 2014; Whipp et al. 2014), or they may be segmented by or completely ignore the pre-existing fault population (e.g. Claringbould et al., 2017; Deng et al., 2017; Henstra et al., 2019). The potential for this structural inheritance of the geometric properties of pre-existing faults by younger ones is governed by multiple factors, including the orientation of the principal stress regime during each rift event (Henza et al., 2011), the magnitude of the prior rift phase (Henstra et al., 2019; Henza et al., 2010), and the mechanical properties of the stratigraphy (Lewis et al., 2013).

When extensional events are greatly separated in time, newly-formed fault populations may be stratigraphically and vertically separated from older, often buried, fault populations, meaning that plan-view relationships may not be informative (Ciftci and Langhi, 2012; Collanega et al., 2019). Furthermore, the presence of ductile units such as salt or shale may vertically partition strain and further decouple fault populations (Lewis et al., 2013). At present, it remains uncertain how strain is distributed and partitioned between vertically separated fault networks, and what effect, if any, the older population may exert over incipient faults in these instances.

In this study, we investigate how a pre-existing fault population at depth influences the development of a stratigraphically shallower fault population, separated by an intervening decoupling interval. More specifically, we examine the causes behind along-strike variations in geometric and kinematic linkage between deep and shallow structural levels, which ultimately influence the degree of structural inheritance expressed in the geometric properties of the shallow fault population. To accomplish this, we analyse a borehole-constrained 3D seismic reflection volume across the Laminaria High along the northern margin of the NW shelf of Australia (Figure 1a). This area is characterised by an E-W oriented fault population at depth, formed during Late Jurassic-Cretaceous extension, overlain by a WSW-ESE oriented fault population at shallow depths formed due to Plio-

Pleistocene lithospheric flexure associated with subduction occurring to the north (Figure 1b) (Ciftci and Langhi, 2012; Keep et al., 2002; Langhi et al., 2011; Langhi and Borel, 2008; Saqab et al., 2017). The shallow grabens often overly the deeper horsts, forming hourglass-type structures, with the two fault populations largely separated by a mechanically incompetent stratigraphic interval (Figure 2a) (Ciftci and Langhi, 2012).

We find that, aside from the collocation of shallow graben above deeper horsts in some areas, the geometry of the shallow fault population is largely independent of the deeper structures, with the shallow faults paralleling the subduction front to the north. However, we note that some older faults extend upwards to shallow depths, producing anomalously oriented structures at shallow depths. We show that the reactivation of deeper faults is modulated by their geometry, with larger structures more likely to reactivate. However, prominent relay zones along the faults may partition reactivated and non-reactivated fault segments, producing areas of hard and soft vertical linkage across the weak interval, respectively. We show how the geometry of deeper faults results in a variable degree of reactivation and linkage between structural levels, influencing the geometry of later-formed structures and exerting a variable degree of structural inheritance over the shallow fault population.

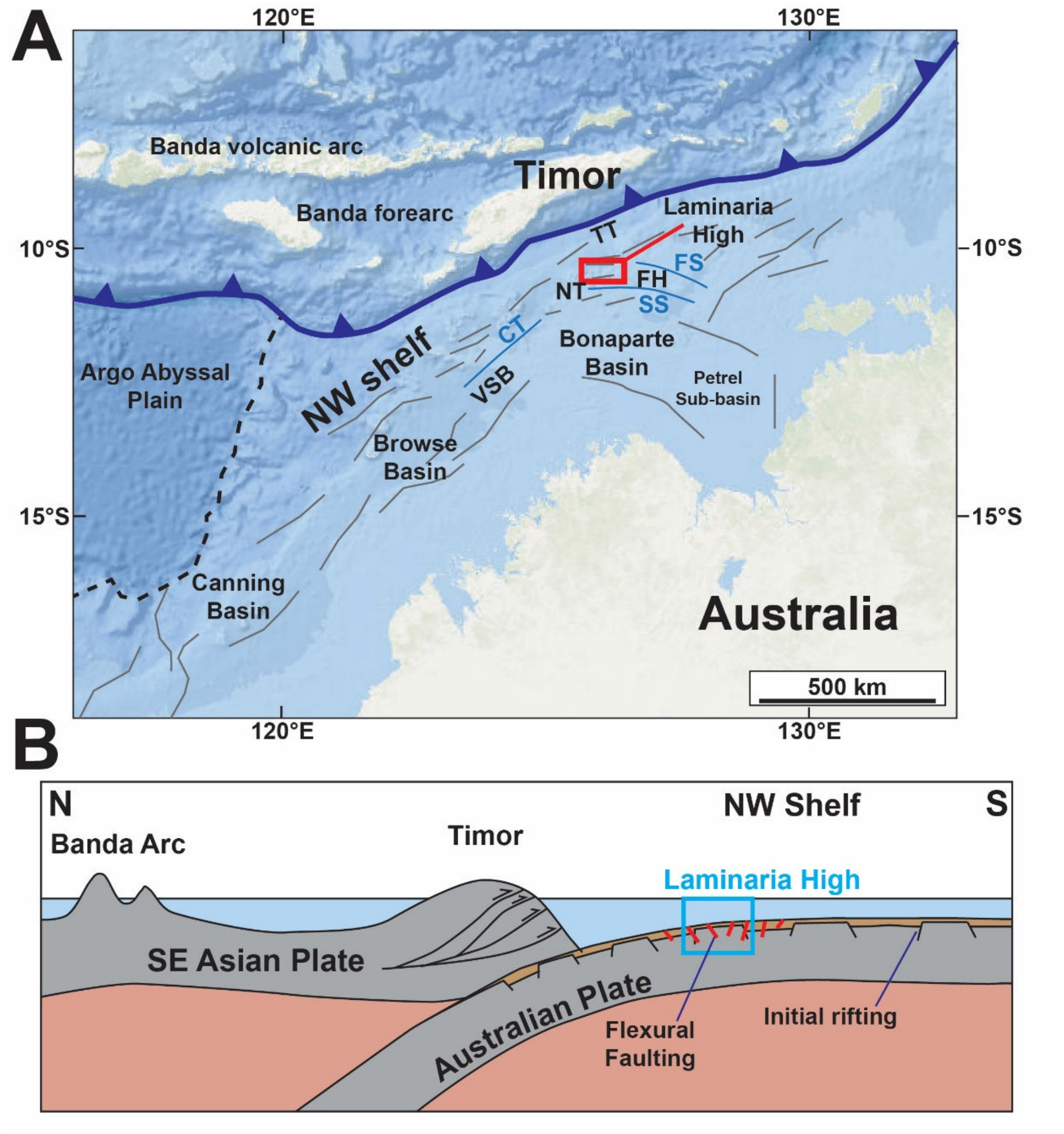

Figure 1 – A) Regional map showing the location of the study area along with key geological features along the NW Shelf of Australia. CT – Cartier Trough; NT – Nancar Trough; TT- Timor Trough; VSB – Vulcan sub-basin; FH – Flamingo High; SS – Sahul Syncline; FS – Flamingo Syncline. Structural elements after Langhi et al., 2013. B) Schematic cross-section highlighting the northern Australian margin being subducted beneath the East Timor subduction zone to the north. Flexural faulting related to this subduction occurs across the Laminaria High. After Ciftci and Langhi, 2012.

2 Geological setting

The Laminaria High is located on the northwest shelf of Australia, along the northern margin of the Bonaparte Basin (Langhi and Borel, 2008; Ciftci and Langhi, 2012). The high is located on the boundary between the continental shelf and slope, which plunges northwards into the East Timor subduction zone (Langhi et al., 2011; Saqab et al., 2017). The study area is bound to the south by the Nancar Trough and Vulcan Subbasin, the Flamingo and Sahul synclines to the east, and the Timor Trough to the north and west (Figure 1a) (Ciftci and Langhi, 2012; Abbassi et al., 2015).

The Bonaparte Basin, including the Laminaria High, experienced three phases of extension throughout its evolution. An initial phase of rifting occurred during the Late Devonian-Early Carboniferous, producing the NW-SE oriented structures adjacent to the Laminaria High, including the Nancar Trough and Flamingo syncline (O'Brien et al., 2013; Langhi and Borel, 2008). A second phase of rifting occurred in the Carboniferous-Permian, associated with the initiation and propagation of the Neo-Tethys rift systems; this rift phase was associated with the formation of the NE-SW oriented Westralian Superbasin across the NW shelf of Australia (Yeates et al., 1987), which includes the Bonaparte, Browse and Canning Basins (Figure 1a) (Jablonski and Saitta, 2004; Langhi and Borel, 2005). A further rift event related to the breakup of Gondwana and associated with the formation of the Argo Abyssal Plain occurred during the Late Jurassic (de Ruig et al., 2000). This latter rift phase imparted a NE-SW oriented fabric across the region, although this was deflected to E-W across the Laminaria High by pre-existing structures associated with the earlier events. Across the Laminaria High this Late Jurassic rift phase was associated with the formation of E-W trending faults, forming the horst and graben rift physiography identified at deep structural levels (Figure 2a). Syn-rift strata deposited during this period comprised the deltaic-to-shallow marine Plover and Laminaria sandstones (Figure 2b) (Abbassi et al., 2015; Labutis and Ruddock, 1998; Ciftci and Langhi, 2012). This extension was also associated with a period of Late Jurassic uplift related to the onset of seafloor spreading (Harrowfield and Keep, 2005)

Following Late Jurassic rifting across the Laminaria High, the area was tectonically quiescent, and a thick shale-dominated interval was deposited throughout the Early Cretaceous (Figure 2b) (Abbassi et al., 2015; Ciftci and Langhi, 2012). Subsequently, accommodation space across the margin was filled by prograding wedges, with the carbonate content increasing upwards through the succession and eventually leading to the establishment of the area as a carbonate platform during the Late Cretaceous, which persisted throughout the Cenozoic (Abbassi et al., 2015; Abdulkareem et al., 2019).

The stratigraphy across the Laminaria High can be broadly divided into three main intervals, syn-rift sandstones associated with Late Jurassic extension at depth, an overlying shale-dominated succession associated with the deepening continental shelf, and the establishment of a carbonate platform during the Cenozoic. Ciftci and Langhi (2012) assign mechanical properties to these broad intervals, suggesting that the shale dominated sequence (H80 to ~H60) represents a mechanically incompetent unit, herein referred to as the MIU, bordered above and below by more competent units dominated by carbonate and sandstone respectively (Figure 2b).

During the Miocene-Pliocene, the northern margin of the Australian Plate collided with the Banda Arc, leading to the onset of subduction and the associated flexure of the downgoing Australian plate to the south (Figure 1b) (Langhi et al., 2011; Saqab et al., 2017). Flexure of the Australian plate led to a prevalent NNW-SSW oriented extension across the Laminaria High, and the formation of WSW-ESE oriented flexural-related faults at shallow depths (Langhi et al., 2011). Some faults extend up to the seabed, indicating that they may be active at the present day. The maximum extension, and likely the peak fault activity, occurred during the Pliocene, when the Laminaria High was situated atop the forebulge of the downgoing plate (Saqab et al., 2017).

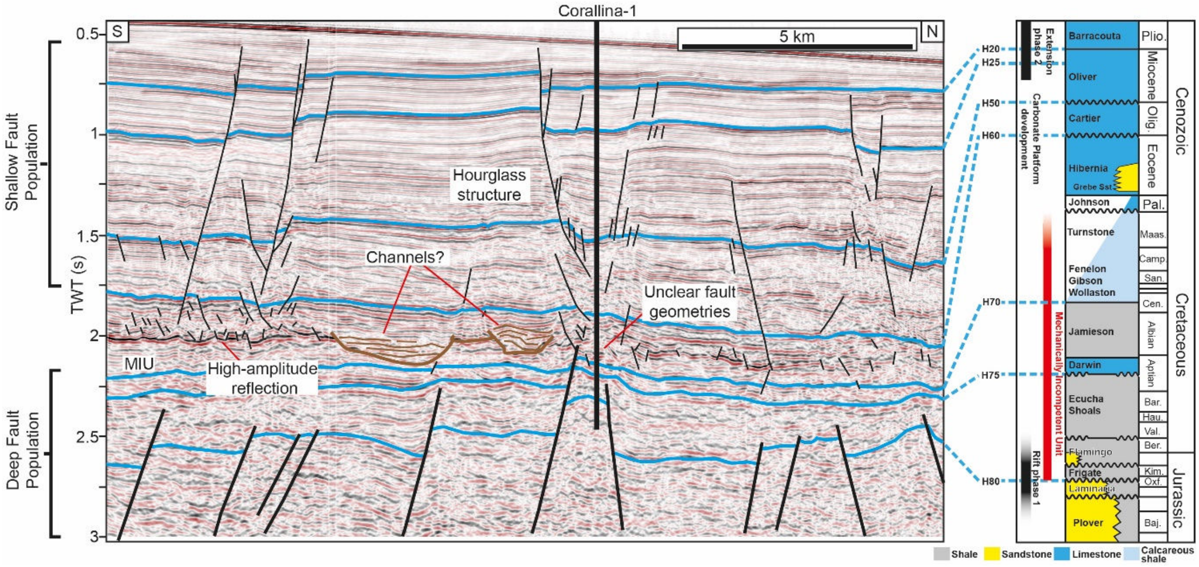

Figure 2 – A) Interpreted seismic section across the Laminaria High, highlighting the Deep and Shallow fault populations and key stratigraphic horizons across the section. The Mechanically incompetent unit (MIU) spans from H80 to above H70. B) Stratigraphic column for the Laminaria High, after Abbassi et al., 2015 and de Ruig et al., 2000. The main rift phases occur in the Late Jurassic and Miocene-Pliocene.

3 Data and Methods

In this study we examine the Laminaria 3D seismic volume covering a ~680 km^2 area of the Laminaria High. The seismic volume records to 3 s TWT depth and has an inline and crossline spacing of 12.5 m. Seismic data are recorded as zero-phase and follow the SEG reverse polarity convention; a downward increase in impedance is represented by a trough (red) whereas a downward decrease in impedance is represented by a peak (black). Seismic imaging is of a good quality across the area, particularly in the shallow section where a high signal-to-noise ratio resolves clearly defined faults (Langhi et al., 2011). Image quality decreases with depth such that interpretations are of lower confidence at deeper levels, although we are able to identify major faults in this interval, in agreement with other studies in the area (Ciftci and Langhi, 2012) (Figure 2a).

We mapped eight borehole-constrained stratigraphic horizons, including the seabed, throughout the volume (Figure 2a). These horizons were constrained by the Vidalia-1, Corallina-1 and Laminaria-1 boreholes, along with information from previous studies in the area (Ciftci and Langhi, 2012). We focussed on mapping prominent reflections throughout the data and subsequently linked our interpretations to the stratigraphic framework provided by de Ruig et al., (2000) and Abbassi et al., (2015). The mapped horizons were: i) Top Oxfordian (H80); ii) Aptian (H75); iii) Cenomanian (H70); iv) Base Oligocene (H60); v) Base Miocene (H50); vi) Late Miocene (H25); vii) Base Pliocene (H20); and viii) the seabed (Figure 2). In addition, we mapped a high-amplitude, laterally discontinuous reflection within the H60-H70 interval where possible, referred to as the High-amplitude reflection.

To examine the evolution of faults and to understand the vertical linkage between the deep and shallow structural levels across the Laminaria High we undertook quantitative fault analyses. Throw-length (T-x) and throw-depth (T-z) plots analyses enable us to elucidate the geometric and kinematic evolution of faults. T-x analyses were undertaken along faults across multiple structural levels (Duffy et al., 2015; Walsh et al., 2003). Measurements were taken at intervals of 50 crosslines intervals (equivalent to 625 m), oriented perpendicular to the main fault strike. By using crosslines, we are able to account for changes in fault orientation at different structural levels and collapse measurements of overlapping fault segments onto a single profile. We also carried out the T-z analyses at multiple points to understand the vertical linkage between the deep and shallow structural levels. Combining this with expansion indices (i.e. the ratio of the hangingwall to footwall thickness) allows us to place this geometric evolution into a temporal framework and to determine when the fault was active. For a specific horizon, throw and expansion indices are plotted at the midpoint between the hangingwall and footwall cutoffs (Baudon and Cartwright, 2008). In order to fully account for all deformation associated with the fault we measure both brittle (faulting of the host rock) and ductile (near-fault folding) components of deformation. To incorporate the ductile folding into our analyses we project horizons towards the fault from areas unaffected by local fault-parallel folding (Duffy et al., 2015; Long and Imber, 2012).

We choose not to depth convert or decompact our data when undertaking fault analyses so as not to introduce additional errors into our measurements. Related to this, we take the vertical component of displacement (fault throw measured in two-way-travel time) rather than displacement to avoid the need to depth convert the data. Due to the relatively layer-cake geometry of the stratigraphy across the Laminaria High, we do not expect any major lateral changes in lithology or velocity structure along the fault. One of the key tenets of our quantitative analyses is that the absolute throw values measured on the plots are less important than their overall shape, it is this latter information that provides key insights into how the faults evolved.

4 Rift physiography

The Laminaria High is characterised by an E-W-trending fault population at deep structural levels, and a WSW-ENE-trending fault population at shallow levels (Figure 3). Here, we describe these fault populations in turn by examining rift physiography across Deep (H80), Intermediate (H75), and Shallow (H25) horizons (Figure 3), before analysing how the fault populations link across these structural levels.

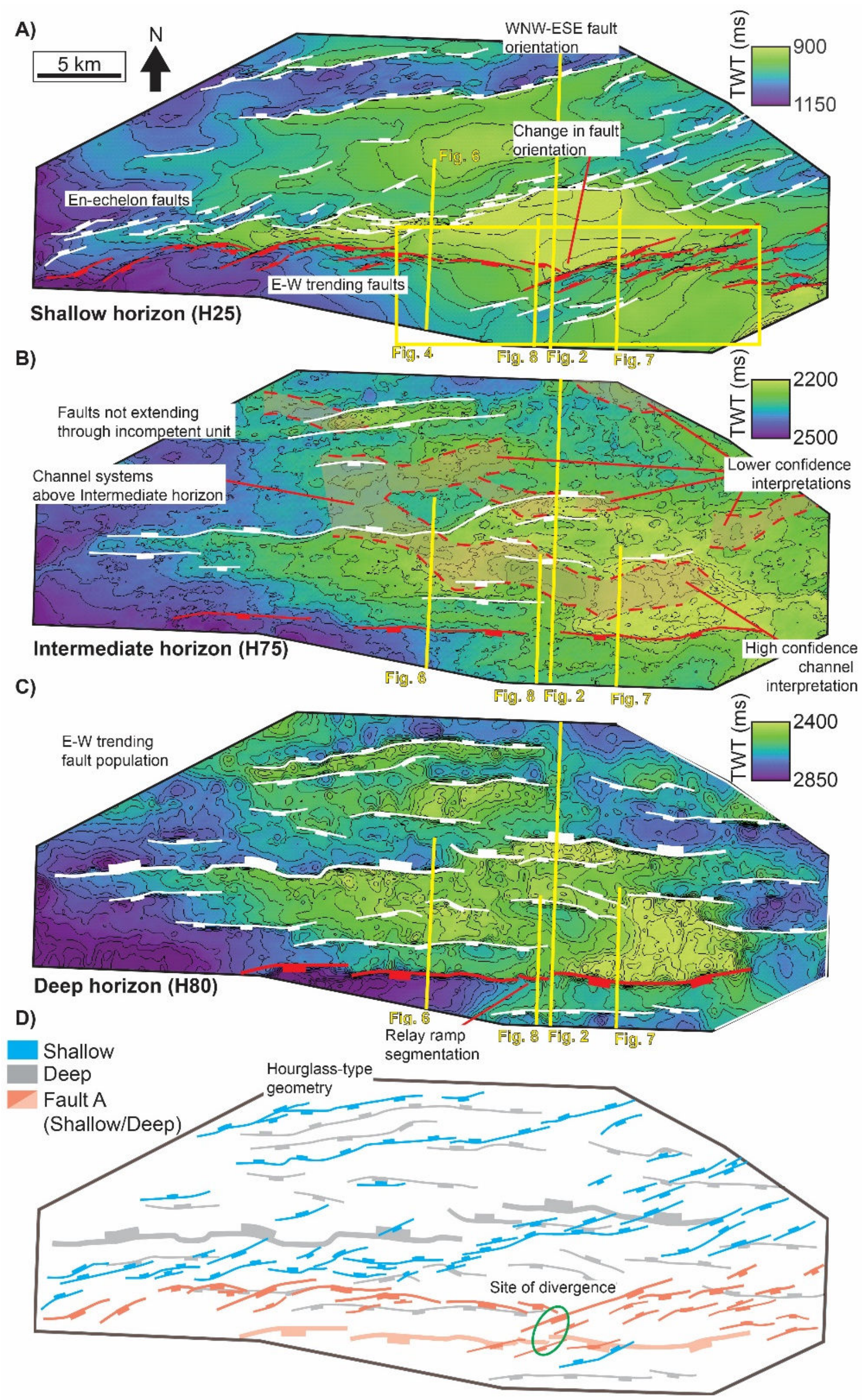

Figure 3 – TWT structure maps of different horizons across the Laminaria High. A) The shallow (H25) horizon. B) Intermediate (H75) horizon. The channels are located above the horizon, see Figure 2. C) E-W-trending faults expressed across the Deep horizon (H80). D) Overlaid faults of the Shallow and Deep Fault populations. Fault A is highlighted in red.

4.1 Basement horizon (H80) – Deep fault population

At deep structural levels, the Laminaria High is characterised by an E-W-striking fault population, herein termed the Deep Fault Population, which we infer formed in response to Late Jurassic rifting across the NW shelf of Australia (Langhi and Borel, 2008). Faults within the Deep population are commonly segmented, with individual segments ~5-10 km in length (Figure 3). The faults define a series of horst and graben, with a large horst present in the south of the area (Figure 3). They typically terminate upwards around the top Albian (H75) horizon (Figure 2a).

4.2 Intermediate horizon (H75) and the Mechanically Incompetent Unit

We take the top Albian (H75) surface to represent the intermediate horizon between the deep and shallow fault populations, and a horizon within the MIU (Figure 2) (Ciftci and Langhi, 2011). Few faults are present across this surface, with only the larger faults of the Deep Fault Population, such as those defining the main horst structures, expressed. Although the majority of faults within the underlying Deep Fault population tip out beneath this horizon (Figure 2), local relief is generated due to differential compaction across the buried faults (Figure 3).

Above the intermediate horizon, we identify a prominent high-amplitude reflection within the MIU (Figure 2a). This horizon displays a negative impedance contrast with respect to overlying strata, is laterally discontinuous, and is offset by numerous small-offset faults that seemingly do not extend far vertically within the section (Figure 2a).

4.3 Shallow Horizon (H25) – Shallow fault population

At shallow depths, the Laminaria High is characterised by a WNW-ESE-trending fault population, which we here term the Shallow Fault Population. These faults formed in response to lithospheric flexure associated with subduction to the north (Saqab et al., 2017). Faults within the Shallow population are typically segmented and often display en-echelon geometries (Figure 3). Towards shallower depths, the faults are also often associated with numerous antithetic and synthetic splays (Figure 2a). Faults within the Shallow Fault Population extend upwards close to the seabed (Figure 2). They typically terminate downwards in the MIU, although individual structures link with the Deep Fault Population (see Fault A on Figure 3).

4.4 Connecting Deep and Shallow structural levels

Horsts and grabens at shallow structural levels are often anti-located above those structures at deeper levels, forming 'hourglass' geometries with shallow grabens overlying deeper horsts in plan-view (Figure 2, 3) (Ciftci and Langhi, 2012). An exception to this in the south of the area, where a large horst is present at both the deep and shallow structural levels, defined by the same E-W-striking faults (Figure 3). We focus on a S-dipping fault along the southern margin of this horst, which is expressed at both the Deep and Shallow structural levels and is here termed Fault A (Figure 3). Within the Deep Fault Population, Fault A forms a ~30 km long E-W-striking structure comprised of at least three ~10 km long segments separated by relay ramps. The western end of the fault extends out of the seismic survey at this depth, although the fault is observed to continue following an E-W orientation westwards across the Intermediate (H75) horizon (Figure 3).

In the west of the area Fault A is expressed within the Shallow Fault Population as an E-W-trending structure. At shallow levels, the E-W orientation of Fault A is anomalous with respect to the prevailing WSW-ENE orientation of the Shallow Fault Population (Figure 3). To the east, the shallow section of Fault A is aligned along a WSW-ENE orientation, with the west and east segments separated by a relay ramp (Figure 4). A similar, although less pronounced, change in orientation from E-W to ENE-WSW also occurs at the western end of Fault A at shallow depths (Figure 3). In the east, both the WSW-ENE-trending shallow segment and the E-W-trending deep segment of Fault A terminate in and are decoupled across the MIU.

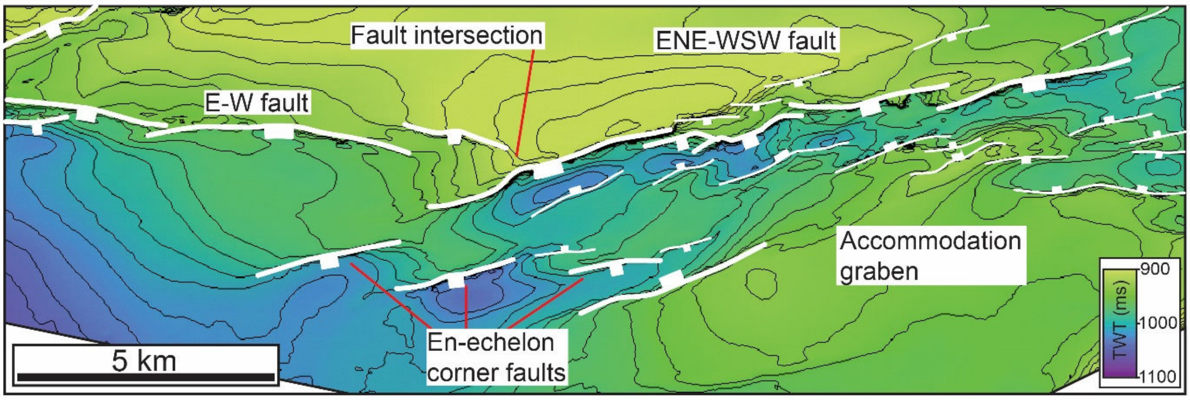

Figure 4 – TWT structure map showing a closeup view of the intersection between the E-W and WSW-ENE segments of Fault A across the Shallow (H25) horizon. See Figure 3a for location.

Across the shallow horizon, the transition from an E-W-striking basement-linked fault segment in the west to a WSW-ENE-striking decoupled fault segment in the east forms a prominent ‘corner-point’, where the E-W section of Fault A in the west terminates in the footwall of WSW-ENE-striking section to the east. There is no lateral geometric linkage between the fault sections across the Shallow horizon, although this does not discount geometric linkage at deeper levels. The relay ramp formed between the two segments dips and widens towards the west (Figure 4). The ENE-WSW section of the fault is associated with a series of en-echelon antithetic faults in its hangingwall, forming a narrow graben. Three S-dipping en-echelon faults are also present in the hangingwall of Fault A, immediately outboard of the intersection. The intersection between the E-W and WSW-ENE fault segments across the Shallow horizon correlates with a relay ramp along Fault A across the Deep horizon, this area is termed the ‘site of divergence’ on Figure 3.

5 Kinematics and vertical coupling along the fault

We undertook T-x and T-z analyses along Fault A. Throw-length (T-x) analyses allowed us to constrain the distribution of throw at various structural levels (Figure 5), whilst throw-depth (T-z) analyses offer insights into how the fault evolved and the degree of coupling between deep and shallow sections of the fault (Figure 6, 7).

Examining the T-x plots, throw along Fault A across the Deep horizon (H80) reaches a maxima of 323 ms in the centre of the fault (crossline 30, ~20 km) (Figure 5). A further maxima of ~258 ms TWT is present towards the east (crossline 51) (Figure 5). No data are available for the western end of the fault across the Deep horizon as the fault extends out of the volume. Multiple throw minima are identified at this depth, likely representing areas of relay ramp segmentation (Figure 3) (e.g. Walsh et al., 2003). A prominent minima of 51 ms throw is present at ~30 km (crossline 46) (Figure 5). Along the Intermediate horizon the throw profile displays two broad maxima of ~100 and ~112 ms TWT at ~20 km (crossline #30) and ~35 km (crossline #52), respectively, separated by a minima of 12 ms at ~30 km (crossline #45). Fault A extends out of the area on this horizon around crossline #11 (~7-8 km).

Throw across the shallow horizon is typically higher than that of the intermediate horizon and less than that of the Deep horizon. Across this surface extension is accommodated by multiple en-echelon fault segments (Figure 5). Individual throw deficits between en-echelon segments are largely removed in the cumulative profile (Walsh et al., 2001). The cumulative throw profile across the Shallow horizon displays two distinct maxima of 135 ms 150 ms at ~12 km (crossline #19) and ~32 km (crossline #48) respectively, separated by a minima of 24 ms at ~28 km (crossline #44). The distribution of maxima and minima along the Shallow horizon is similar to that of the intermediate horizon. A commonality between the displacement profiles is the presence of an area of low throw around 30 km along the length of the fault (around crossline #45). This corresponds to the site of divergence along Fault A, represented by a relay ramp at the Deep horizon, and the corner point on the shallow horizon (Figure 3, 4). Across the Shallow horizon, this common minima separates the hard-linked E-W segment of Fault A in the west from the soft-linked decoupled section of the fault in the east.

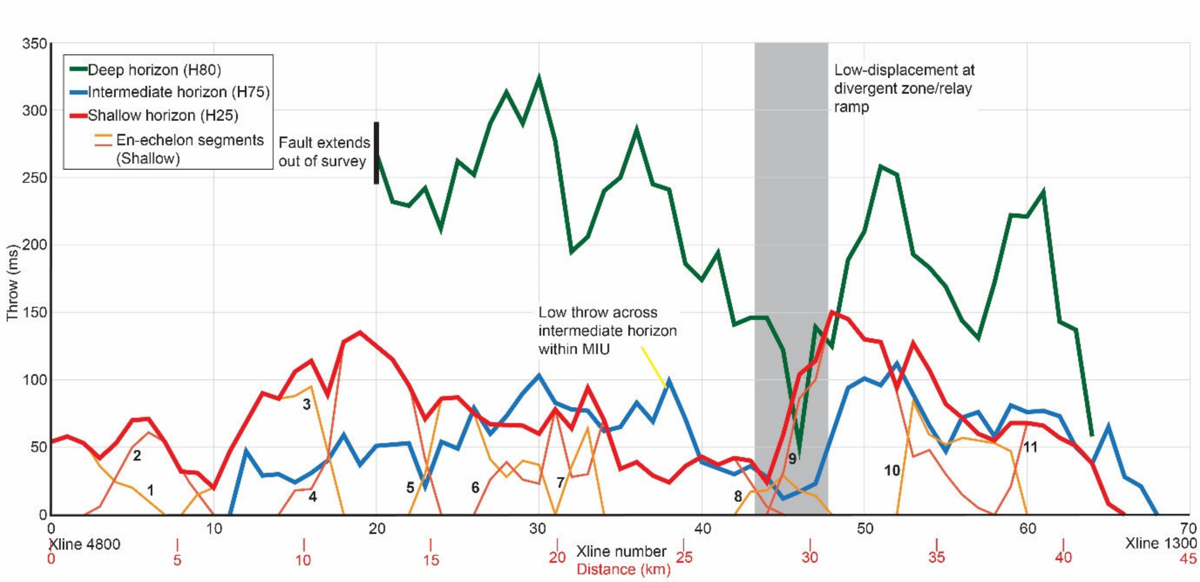

Figure 5 – Throw-length plots along Fault A across the Deep, Intermediate and Shallow horizons. Throw measurements were calculated along the same xlines to allow for comparison. The fault at the Deep horizon extends out of the seismic volume in the west. Indiivudal segments of the fault at Shallow depths are shown in orange and pink, with the cumulative throw shown in red.

5.1 Hard-linked fault segment

In the west, Fault A forms an E-W-striking structure that extends throughout the section and links the Deep and Shallow fault populations. Similarly, a N-dipping fault on the northern margin of the horst also extends displays an E-W strike and extends through the MIU towards shallower depths, although this does not reach the Shallow Horizon as a single structure (Figure 3, 6). Fault A displays an en-echelon geometry toward shallow depths with few associated antithetic faults. Throw-depth analyses show a maxima of ~250 ms within the Jurassic interval at ~2.5 s TWT, with a long tail of ~50 ms throw extending upwards for 2 s TWT to just beneath the present-day seabed (Figure 6). High-amplitudes across the seabed likely represent carbonate cementation following fluid flow along the faults, suggesting that, at the sub-seismic scale, these faults likely reach the seabed (Abdulkareem et al., 2019). Expansion indices display a maxima of ~2.1 at deeper levels (2.5-3 s TWT) and remain ~1 towards the upper fault termination. The throw maxima in the Jurassic interval indicates that the fault initiated in this interval. In addition, the thickening of the Jurassic interval into the hangingwall of the fault and the associated high expansion index indicates the fault was active at this time; we suggest this activity likely corresponds to the regional Late Jurassic rift phase (Figure 6). We interpret that the low throw fault upper tail corresponds to a period of later activity as the fault was reactivated and propagated upwards through the succession. We relate this later reactivation to Pliocene-Pleistocene extension in response to regional subduction-related flexure (Figure 1b). Subtle hangingwall thickening and slightly elevated expansion indices at shallow levels may corroborate this interpretation although they are not conclusive.

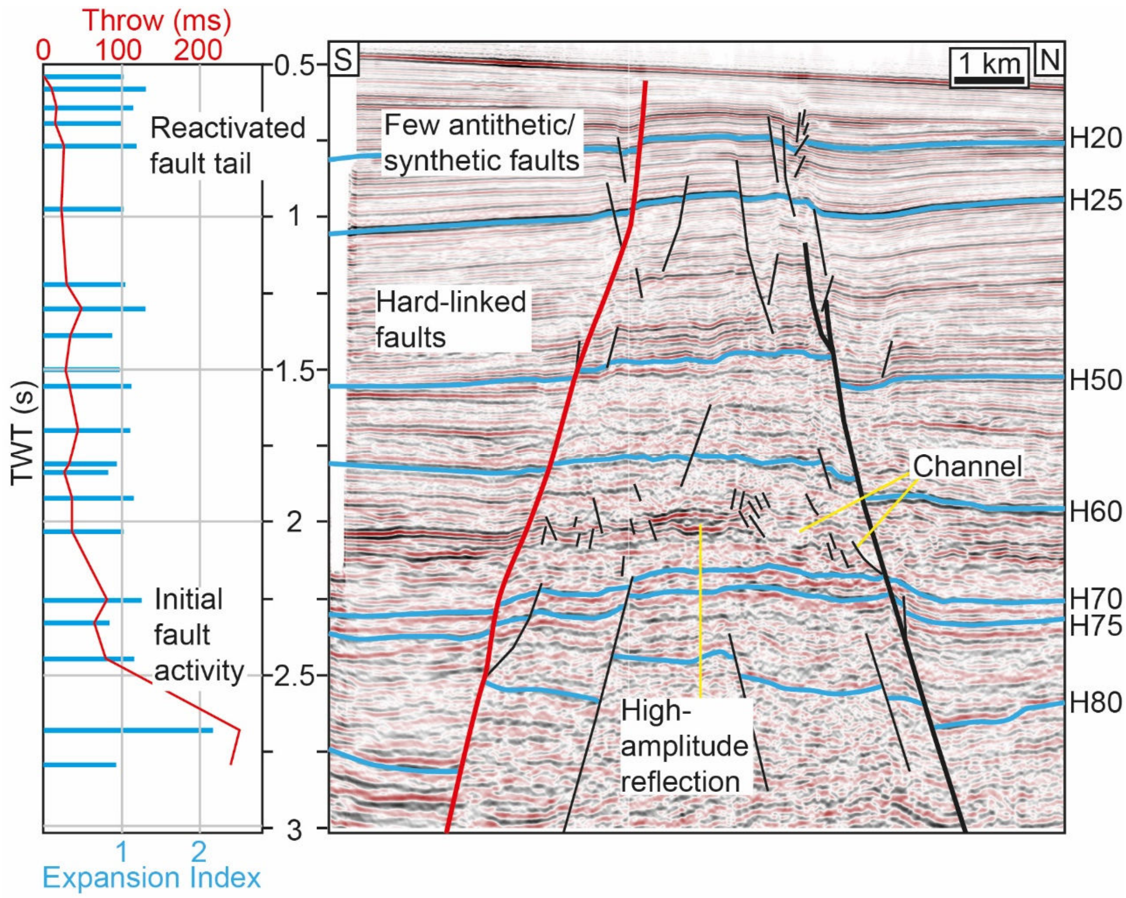

Figure 6 – Interpreted seismic section and throw-depth plot of the hard-linked section of Fault A (red) in the west of the area. See figure 3 for location.

5.2 Soft-linked WSW-ENE fault segment

In contrast to the western section of the fault, there is no geometric linkage between the E-W-striking section of Fault A at Deep structural levels and the WSW-ENE-striking shallow section of Fault A in the east. Here, the Deep section of the fault terminates upwards within the MIU, whilst the shallow section terminates downwards at around 1.6 s TWT, above the H60 horizon and the MIU. The shallow fault section is associated with numerous antithetic fault segments. The area between the fault segments is characterised by a high-density of low-displacement, vertically-restricted faults (Figure 7). We note that the High-amplitude reflection shows no significant offset related to either the Deep or Shallow sections of the fault, suggesting no geometric linkage between the two.

Throw-depth analyses highlight a throw maxima of ~200 ms at ~2.5 s TWT within the Jurassic interval, similar to the hard-linked segment of the fault to the west. The expansion index at this depth reaches ~2, again similar to the western segment. The T-z plot for the shallow section of the fault is characterised by a single throw maxima in the centre (~60ms TWT at 1.25 s TWT), decreasing to zero at its upper and lower tips (~0.5 and ~1.5 s TWT respectively). Expansion indices cluster around 1 throughout this interval although they increase to around ~1.5 above 0.75 s TWT, above the Base Pliocene (H20) horizon (Figure 7).

The Jurassic throw maxima and high expansion index at depth suggest late Jurassic activity along the fault, as identified along the hard-linked fault segment to the west (Figure 6). Similarly, based on the high expansion index above H20, we suggest that the shallow section of the fault formed in response to Pliocene-Pleistocene extension. However, in contrast to the western section of the fault, we suggest that this formed as a blind structure, initiating around the shallow throw maxima, rather than the upward propagation of the basement fault section (Figure 7). The zone of complex faulting between the shallow and deep sections of the fault in this area suggests soft-linkage and some strain transfer through the MIU.

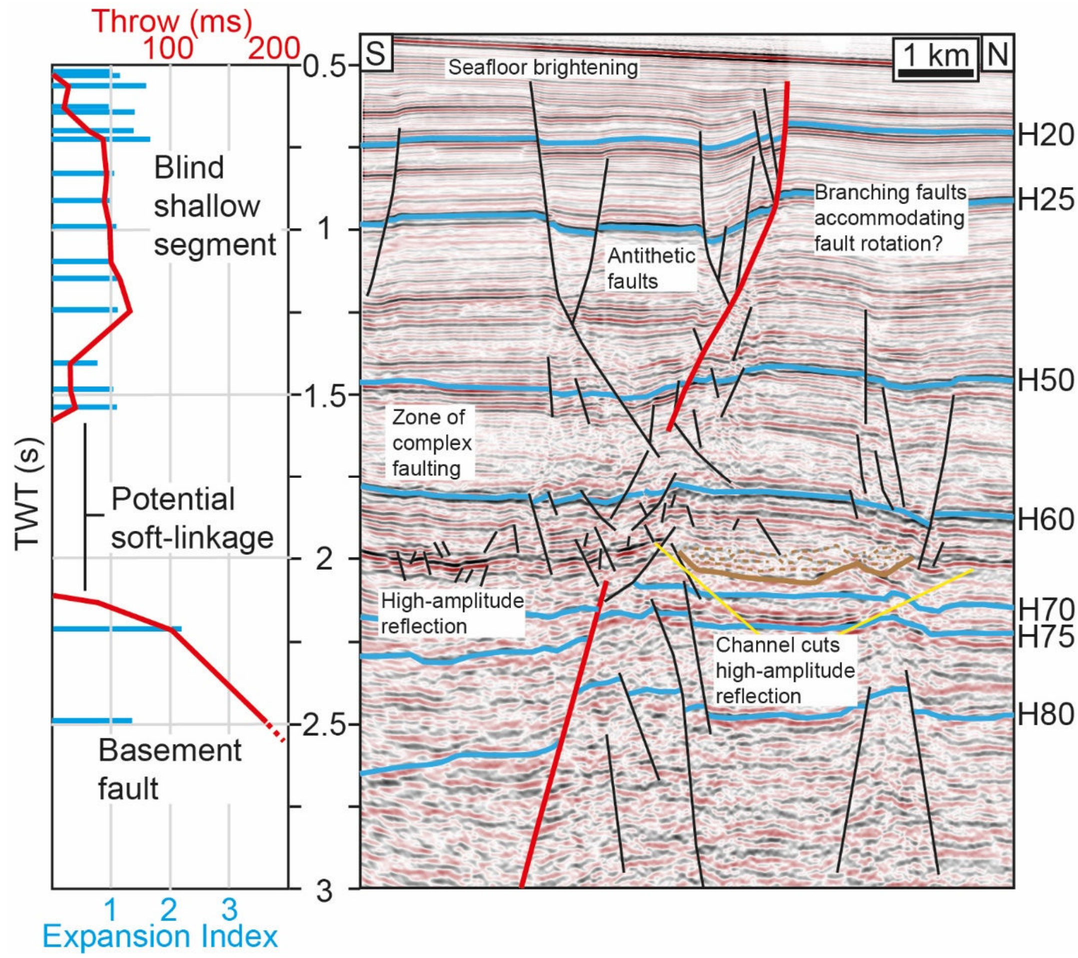

Figure 7 – Interpreted seismic section and throw-depth plot of the soft-linked section of Fault A (red) in the east of the area. See Figure 3 for location.

5.3 En-echelon faults

Three en-echelon faults are located in the hangingwall of Fault A, outboard of the intersection between the E-W and ENE-WSW oriented fault segments (Figure 4). These right-stepping, S-dipping faults are within the Shallow Fault Population only and do not link to any faults in the Deep Fault Population, instead terminating at depth above the MIU (Figure 8). The vertical linkage between the Deep section of Fault A and the ENE-WSW and E-W shallow sections cannot be resolved in this area.

Kinematic analyses of the central en-echelon fault shows a bell-shaped displacement profile with a throw maxima of ~65 ms from 1-1.25 s TWT, decreasing to zero at the upper (~0.5 s TWT) and lower (1.75 s TWT) tips of the fault. Based on i) the lack of distinct growth strata in the hangingwall of the fault; ii) the relatively constant expansion index of ~1 along the fault; and iii) the bell-shaped displacement curve, we interpret that this fault formed as a blind structure in the hangingwall of Fault A (Figure 4, 8).

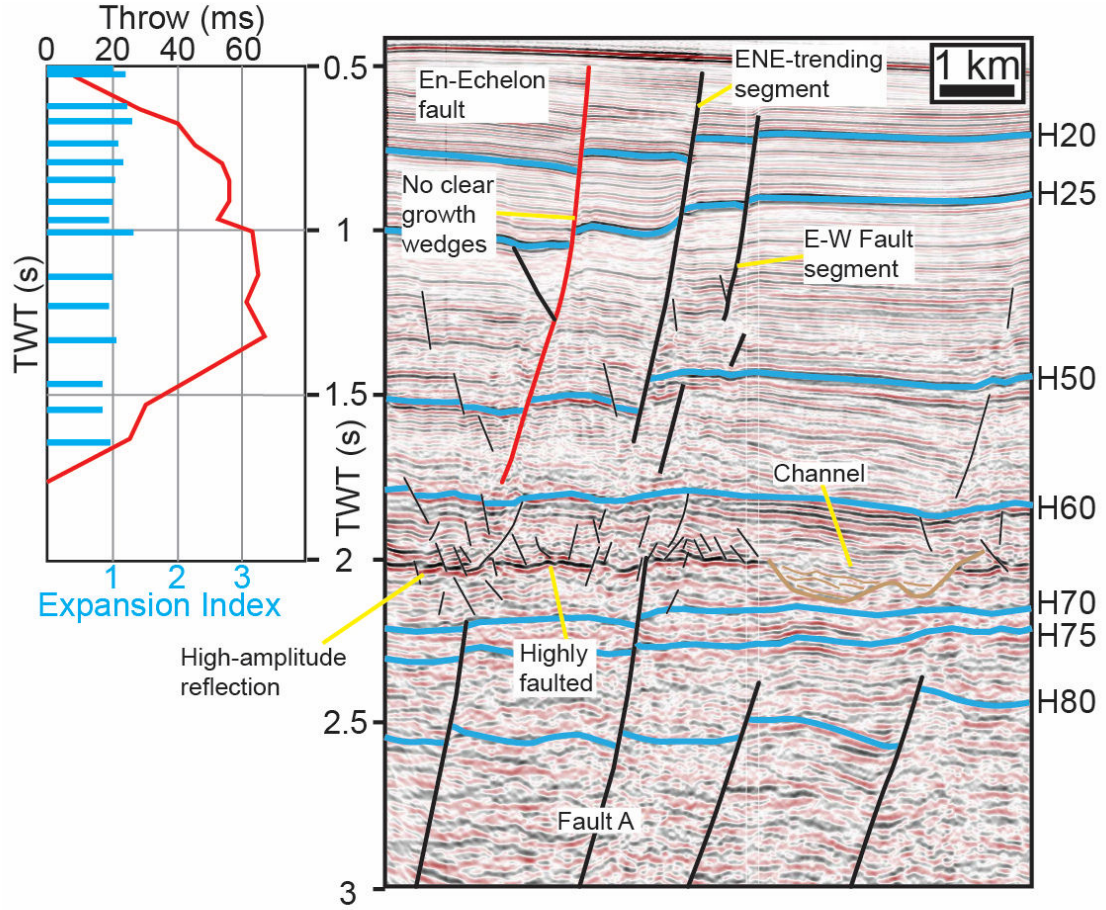

Figure 8 – Interpreted seismic section and throw-depth plot of the central en-echelon fault segment (red), located in the hangingwall of Fault A. See figure 3 for location.

6 Discussion

We have documented along-strike changes in the reactivation of a buried, pre-existing fault, and its coupling with younger faults at shallow depths. We find that this change in vertical coupling and reactivation influences the degree of structural inheritance that we identify within the later-formed Shallow Fault Population. This variation in coupling between shallow and deep fault populations is modulated by a mechanically weak intervening stratigraphic interval. Here, we first discuss the geometry and character of this mechanically weak interval (the MIU), before discussing vertical coupling between the shallow and deep fault populations, and how strain is partitioned laterally between the E-W and WSW-ENE segments within the Shallow Fault population.

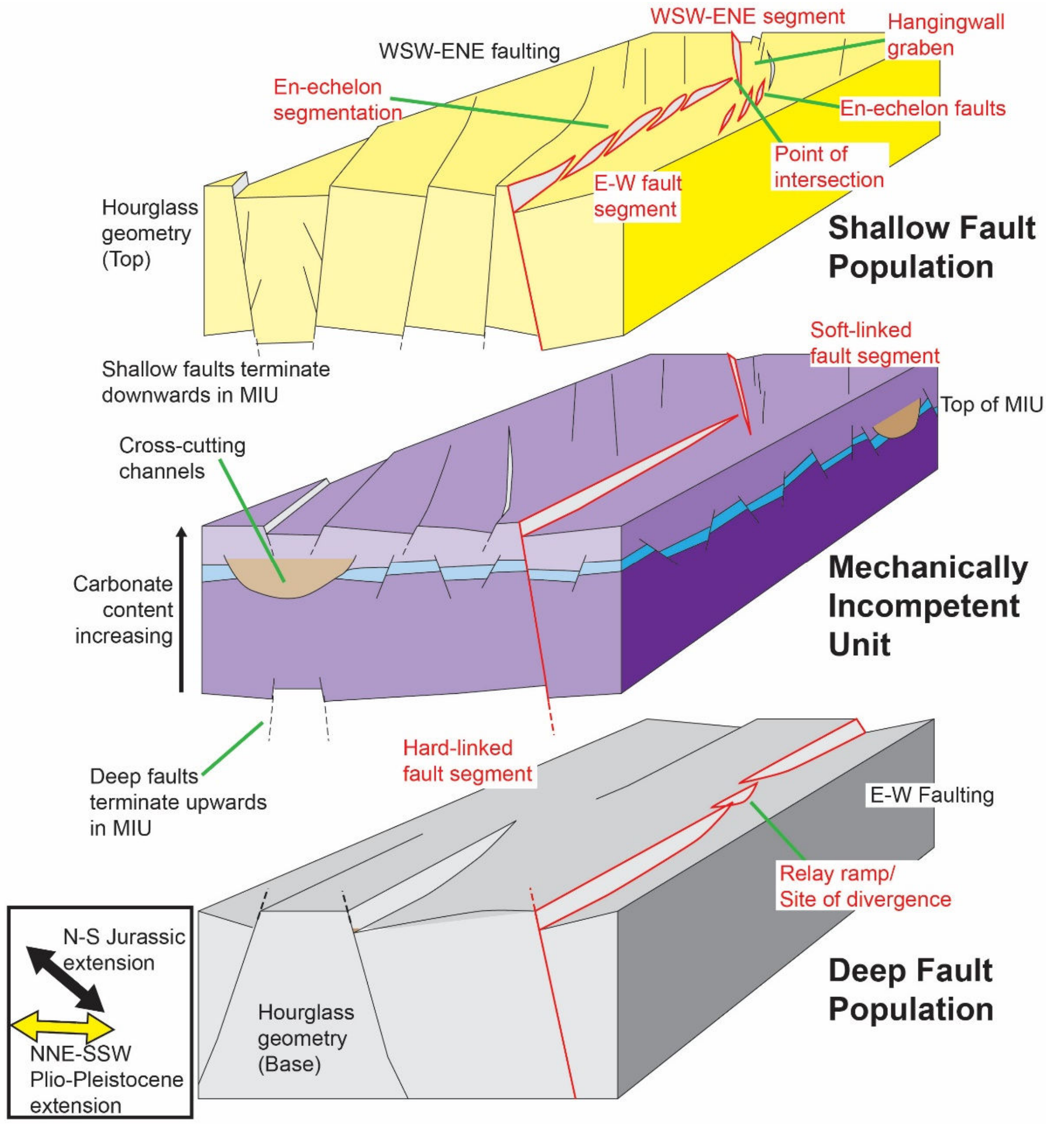

Figure 9 – Schematic block model showing the different structural levels and fault populations across the Laminaria high, along with the relationships between them. Faults within the deep and shallow fault populations terminate at the base and top of the MIU respectively, with the exception of Fault A, shown in red.

6.1 Geometry and composition of the Mechanically Incompetent Unit

The Deep Fault Population is decoupled from the Shallow Fault population across the Laminaria High by a mechanically incompetent, shale-dominated stratigraphic interval termed the MIU (Figure 2, 9) (Ciftci and Langhi, 2012). This interval spans Late Jurassic to Paleocene strata and is 0.75-1 s TWT thick across the area (Figure 2). Faults of the Deep Fault Population terminate upwards at the base of the MIU around the H75 horizon, whereas those in the shallow population terminate downwards into the top of the MIU around the Late Cretaceous-Early Cenozoic interval (H60) (Figure 2). The composition and geometry of the MIU varies laterally and with depth across the Laminaria High. Based on uniaxial compressive strength as calculated from p-wave sonic logs, Ciftci and Langhi (2012) define a ~500m thick incompetent interval beginning at H80 and extending upwards to between H70 and H60 (Figure 2). In addition, the weakest interval within the MIU, corresponding to a claystone interval, is situated below the H70 horizon and above the Valanginian Unconformity, located between H75 and H80.

We identify a prominent high-amplitude reflection between H70 and H60, seemingly located towards the top of the MIU (Figure 2). The reflection is characterised by a high amplitude and negative impedance contrast, is offset by numerous low-displacement faults that do not extend vertically into the section, and is laterally discontinuous over 2-3 km intervals (Figure 2, 7). We note that the distribution of faulting is greater above the high-amplitude reflection than below (Figure 2, 7, 8), with the fault density greatest at areas of interaction between the Shallow and Deep Fault populations. In addition, the reflection is strata-concordant and often separates reflective strata above from more acoustically transparent strata below (Figure 8). The high-amplitude and negative polarity of the reflection indicate a relatively abrupt downwards decrease in acoustic impedance. Based on this, we suggest that the high-amplitude reflection represents an interface between relatively competent and strong carbonates above and a weaker shale-dominated interval below. This may represent a shelf-slope break unconformity at the Base Cenozoic and the top of the MIU (Figure 2b) (Abbassi et al., 2015). Diagenetic processes occurring at this time may have led to the development of a hardground, producing the observed high-amplitude reflection. In addition, we suggest that the low-displacement faults offsetting the horizon represent a transition between strain being accommodated by large, localised faults in the stronger intervals above, diffuse faulting approaching the MIU, with ductile strain dominant within the MIU itself. The laterally discontinuous nature of the High-amplitude reflection appears to relate to later truncation by E-W-trending channel systems (Figure 2, 7, 8). These channels are ~0.1 s TWT deep, 1-2 km wide and are characterised by low-amplitude reflectivity that onlap the channel margin (Figure 6, 8). We speculate that these channel systems may correspond to the Eocene Grebe sandstone (Figure 2b) (Abbassi et al., 2015), with the Laminaria High representing a relatively shallow marine environment at the time.

6.2 Vertical decoupling of structural inheritance

Although the MIU largely decouples the Deep and Shallow fault populations across the Laminaria High, the presence of ‘hour-glass’ structures, where shallow graben are collocated above deeper horsts, suggests some strain transference vertically between intervals. Fault A forms an E-W-trending structure in the west, extending through the MIU and connecting Deep and Shallow fault populations (Figure 6, 9). In contrast, the Shallow and Deep segments of Fault A are decoupled across the MIU to the east, with the shallow segment displaying a WSW-ENE orientation (Figure 7). This change in fault style suggests that the degree of strain transfer vertically across the MIU changes along Fault A.

During Plio-Pleistocene extension, faults in the Deep Fault Population likely experienced some reactivation although upwards propagation of these faults was inhibited by the MIU, which accommodated strain in a ductile manner (Figure 9). Rather than the reactivation of deeper structures, strain during Plio-Pleistocene extension was largely accommodated by faults that nucleate at shallow depths. Furthermore, as Plio-Pleistocene extension was associated with regional subduction-related flexure to the north (Saqab et al., 2017), faulting may be enhanced and promoted at shallow depths, as opposed to the reactivation of deeper structures, due to outer-arc extension. An exception to this is Fault A, where reactivation of the deep section of the fault occurs in the west and soft-linkage between Deep and Shallow fault sections occurs in the east; a key question therefore, is what drives this along-strike change in vertical coupling along Fault A?

The thickness of the MIU changes regionally across the Laminaria high, thinning towards the North and east. A thicker incompetent interval may more efficiently partition strain and decouple fault populations. The thickness of ductile salt intervals has been shown to exert a strong control on strain transfer between sub- and supra-salt fault systems, with thicker ductile intervals promoting increased decoupling (Lewis et al., 2013). Similarly, albeit at a much larger scale, analogue modelling of crustal processes highlight how thick and weak lower crustal intervals effectively partition the strong upper mantle from the brittle upper crust (Zwaan et al., 2021). However, although the thickness of the MIU changes across the area, this does not correlate with any systematic variation in coupling between shallow and deep fault populations (Figure 3). For example the reactivated western segment of Fault A extends through the supposedly thicker section of the MIU in the west. Lateral lithological changes within the MIU, such as truncation by channels, effectively reduce the thickness of the MIU and may cause abrupt changes in its overall competency. However, we identify no channel features in the area of the intersection point (Figure 3b). These observations suggest that lateral changes in the competency of the MIU do not account for the abrupt along-strike transition from soft- to hard-linkage observed along Fault A.

In the Deep Fault population, Fault A displays two throw maxima, separated by a prominent minima at ~30 km distance along the fault that persists in the same location across all structural levels (Figure 5). Across the Deep horizon it corresponds to a relay ramp along the fault whilst at shallow depths, it corresponds to the intersection points between the E-W and WSW-ENE-trending fault segments (Figure 4). The relay ramp across the Deep horizon may contain an internal small fault segment, although this is difficult to resolve, and may also be located between two underlapping segments (Figure 3).

Fault A forms the southern border to one of the largest horsts in the area, with throw across the Deep horizon greatest to the west of the relay ramp (Figure 3, 5). Observations regarding the evolution of normal fault systems and potential inversion suggest that larger structures are more likely to localise strain and reactivate than smaller ones (Walsh et al., 2001; Reilly et al., 2016). Fault A forms one of the largest faults across the Laminaria High, forming the southern boundary to a large horst. The highest throw along the fault occurs across the Deep horizon to the west of the relay ramp, i.e. the segment that was reactivated (Figure 3, 5). Accordingly, we suggest that Fault A, and in particular its western segment, may represent one of those most likely to reactivate. Similarly, the northern boundary fault to this horst also appears to reactivate and propagate through the MIU (Figure 6).

We suggest that the high-displacement, western segment of Fault A reactivated during Plio-Pleistocene extension and was able to propagate upwards through the MIU, forming an anomalously oriented structure within the Shallow Fault Population (Figure 3, 6, 9). The geometric complexity of a structure may also impact its likelihood to reactivate (Phillips et al., 2020). We suggest that the relay ramp along Fault A acted as a buffer to the reactivation and upwards propagation of the deep section of Fault A further east, where upwards propagation was inhibited by the MIU (Figure 9). Langhi and Borel (2008) identify a series of transverse accommodation zones located between E-W fault segments that they relate to the initial propagation and segmentation of the Deep Fault Population. However, we speculate that such structures and the associated relay ramps may represent a manifestation of a deeper fabric, controlling both the initial location of the accommodation zone and therefore the subsequent relay. Such a mechanism would potentially explain why the change in structural styles occurs in these locations and not at other relay ramps, although we are unable to confirm this.

Soft-linkage between Shallow and Deep sections of Fault A occurs east of the relay ramp. The shallow segment of Fault A strikes WSW-ENE, with a series of en-echelon antithetic faults forming a hanging wall graben to the south (Figure 4, 7). We suggest that this antithetic graben forms to accommodate strains associated with the continued eastwards divergence of the shallow and deep fault segments. As the shallow and deep fault segments diverge, the degree of linkage between them diminishes. At the western end of Fault A, the shallow section of the fault also begins to rotate to a more WSW-ENE orientation. In this instance, we suggest that the deep section of the fault is no longer present, having terminated further east, allowing the shallow section to rotate into the regional stress field.

6.3 Strain accommodation along optimally and non-optimally oriented faults

The shallow section of Fault A in the west is anomalously oriented with respect to others in the Shallow Fault Population (Figure 3, 9). (Figure 9). The majority of faults within the Shallow fault population, including the eastern shallow segment of Fault A, are oriented WSW-ENE, paralleling the subduction zone to the north (Figure 1). Non-optimally oriented faults, such as the western segment of Fault A, may locally reorient the regional stress field, such that they experience dip-slip activity, as observed in the East African Rift (Philippon et al., 2015) and onshore Norway (Fossen et al., 2016). Alternatively, strain may be partitioned into strike-slip and dip-slip components such that the fault experiences oblique slip (Giba et al., 2012; Phillips et al., 2018). We note that the western segment of Fault A is highly segmented, with individual segments displaying an en-echelon geometry (Figure 3). En-echelon fault geometries may form through the oblique reactivation of a pre-existing fault (Giba et al., 2012; Grant and Kattenhorn, 2004; Withjack et al., 2017), or dip-slip activity within a mechanically anisotropic unit (Jackson and Rotevatn, 2013; Schopfer et al 2007). Aside from the broad changes in mechanical strength through the section illustrated by the MIU, we do not see such anisotropy within the stratigraphy at shallow depths. In addition, the WSW-ENE-trending faults in the north of the area display a much more linear geometry (Figure 3). Accordingly, we suggest that the en-echelon geometry of the western segment of Fault A indicates oblique reactivation of the deeper fault. Although the fault displays an overall E-W orientation, each individual segment displays a more optimal geometry as it rotates toward the regional stress field at its tips. As well as a transition from hard- to soft-linkage, the corner-point also represents a transition from oblique activity in the west to dip-slip activity in the east, at least at shallow depths. This area is associated with three en-echelon faults outboard of the corner-point and a high density of faulting immediately above the MIU (Figure 8). Based on this, we suggest that the cornerpoint between the E-W and WSW-ENE fault segments represents an increased concentration of stresses, accommodating the transition between the optimally and non-optimally oriented structures (Figure 9). These faults accommodate increased stresses associated with the transition from oblique to dip-slip activity, perhaps serving a similar function to release faults identified in the hangingwall of larger structures (Destro, 1995). Similar examples where hangingwall faults accommodate stresses associated with changes in fault orientation have been documented in the North Sea (Phillips et al., 2018).

7 Conclusions

In this study we document the geometric and kinematic evolution of a reactivated, buried fault in the Laminaria High, highlighting how vertical coupling along the fault changes along-strike, influencing the degree and style of structural inheritance that occurs in the shallow fault population. We find that:

- The Laminaria high is characterised by an E-W-trending fault population at depth formed during Late Jurassic rifting, and a WSW-ENE fault population at shallow depths formed due to flexure associated with the Timor Subduction zone to the north. These fault populations are vertically separated and decoupled across a mechanically incompetent unit comprised predominately of shales.
- Some faults in the area extend through the mechanically incompetent interval, of which we focus on one fault in particular, Fault A. At shallow depths, the western segment of the fault is oriented E-W following the orientation of the Deep Fault population, whereas the eastern segment is not geometrically linked and displays a WSW-ENE orientation, mirroring other faults in the Shallow Fault Population
- This along-strike change in the degree of vertical coupling corresponds to an area of low-displacement and a relay ramp along the fault. We suggest that the reactivation and upwards propagation of Fault A in the west is inhibited further east at a relay ramp along the fault. Past the relay ramp, the shallow and deep segments display no geometric linkage although some strain transfer and soft-linkage is present. The eastwards divergence of the shallow and deep segments is accommodated by a series of antithetic faults.
- Stresses associated with the transition between the non-optimally-oriented E-W fault segment in the west, to the more optimal WSW-ENE segment in the east are accommodated by a

series of en-echelon structures formed outboard of the intersection between the two fault segments.

References

Abbassi, S., di Primio, R., Horsfield, B., Edwards, D. S., Volk, H., Anka, Z., & George, S. C. (2015). On the filling and leakage of petroleum from traps in the Laminaria High region of the northern Bonaparte Basin, Australia. Marine and Petroleum Geology, 59, 91-113. https://doi.org/10.1016/j.marpetgeo.2014.07.030

Abdulkareem, L., Imber, J., & Hobbs, R. (2019). Geophysical evidence for structurally-controlled, authigenic carbonate cementation in the Laminaria High, Bonaparte basin, Northwest Shelf of Australia. Marine and Petroleum Geology, 99, 563-576. https://doi.org/10.1016/j.marpetgeo.2018.10.018

Baudon, C., & Cartwright, J. (2008). The kinematics of reactivation of normal faults using high resolution throw mapping. Journal of Structural Geology, 30(8), 1072-1084. https://doi.org/10.1016/j.jsg.2008.04.008

Çiftçi, N. B., & Langhi, L. (2012). Evolution of the hourglass structures in the Laminaria High, Timor Sea: Implications for hydrocarbon traps. Journal of Structural Geology, 36, 55-70. https://doi.org/10.1016/j.jsg.2011.12.006

Claringbould, J. S., Bell, R. E., Jackson, C. A. L., Gawthorpe, R. L., & Odinsen, T. (2017). Pre-existing normal faults have limited control on the rift geometry of the northern North Sea. Earth and Planetary Science Letters, 475, 190-206. https://doi.org/10.1016/j.epsl.2017.07.014

Collanega, L., Siuda, K., Jackson, C. A. L., Bell, R. E., Coleman, A. J., Lenhart, A., ... & Breda, A. (2019). Normal fault growth influenced by basement fabrics: The importance of preferential nucleation from pre-existing structures. Basin Research, 31(4), 659-687. https://doi.org/10.1111/bre.12327

Deng, C., Fossen, H., Gawthorpe, R. L., Rotevatn, A., Jackson, C. A., & FazliKhani, H. (2017). Influence of fault reactivation during multiphase rifting: The Oseberg area, northern North Sea rift. Marine and petroleum geology, 86, 1252-1272. https://dx.doi.org/10.1016/j.marpetgeo.2017.07.025

Destro, N. (1995). Release fault: A variety of cross fault in linked extensional fault systems, in the Sergipe-Alagoas Basin, NE Brazil. Journal of Structural Geology, 17(5), 615-629. https://doi.org/10.1016/0191-8141(94)00088-H

Duffy, O. B., Bell, R. E., Jackson, C. A. L., Gawthorpe, R. L., & Whipp, P. S. (2015). Fault growth and interactions in a multiphase rift fault network: Horda Platform, Norwegian North Sea. Journal of Structural Geology, 80, 99-119. https://doi.org/10.1016/j.jsg.2015.08.015

Fossen, H., Khani, H. F., Faleide, J. I., Ksienzyk, A. K., & Dunlap, W. J. (2017). Post-Caledonian extension in the West Norway–northern North Sea region: the role of structural inheritance. Geological Society, London, Special Publications, 439(1), 465-486. https://doi.org/10.1144/SP439.6

Giba, M., Walsh, J. J., & Nicol, A. (2012). Segmentation and growth of an obliquely reactivated normal fault. Journal of Structural Geology, 39, 253-267. https://doi.org/10.1016/j.jsg.2012.01.004

Grant, J. V., & Kattenhorn, S. A. (2004). Evolution of vertical faults at an extensional plate boundary, southwest Iceland. Journal of Structural Geology, 26(3), 537-557.

Harrowfield, M., & Keep, M. (2005). Tectonic modification of the Australian North-West Shelf: episodic rejuvenation of long-lived basin divisions. Basin Research, 17(2), 225-239. https://doi.org/10.1111/j.1365-2117.2005.00251.x

Henstra, G. A., Kristensen, T. B., Rotevatn, A., & Gawthorpe, R. L. (2019). How do pre-existing normal faults influence rift geometry? A comparison of adjacent basins with contrasting underlying structure on the Lofoten Margin, Norway. Basin Research, 31(6), 1083-1097. https://doi.org/10.1111/bre.12358

Henza, A. A., Withjack, M. O., & Schlische, R. W. (2010). Normal-fault development during two phases of non-coaxial extension: An experimental study. Journal of Structural Geology, 32(11), 1656-1667. https://doi.org/10.1016/j.jsg.2009.07.007

Henza, A. A., Withjack, M. O., & Schlische, R. W. (2011). How do the properties of a pre-existing normal-fault population influence fault development during a subsequent phase of extension?. Journal of Structural Geology, 33(9), 1312-1324.

Jablonski, D., & Saitta, A. J. (2004). Permian to Lower Cretaceous plate tectonics and its impact on the tectono-stratigraphic development of the Western Australian margin. The APPEA Journal, 44(1), 287-328. https://doi.org/10.1071/AJ03011

Jackson, C. A. L., & Lewis, M. M. (2016). Structural style and evolution of a salt-influenced rift basin margin; the impact of variations in salt composition and the role of polyphase extension. Basin Research, 28(1), 81-102.

Keep, M., Clough, M., & Langhi, L. (2002). Neogene tectonic and structural evolution of the Timor Sea region, NW Australia.

Labutis, V. R., & Ruddock, A. D. (1998). Stratigraphy of the southern Sahul Platform. The APPEA Journal, 38(1), 115-136. https://doi.org/10.1071/AJ97006

Langhi, L., & Borel, G. D. (2005). Influence of the Neotethys rifting on the development of the Dampier Sub-basin (North West Shelf of Australia), highlighted by subsidence modelling. Tectonophysics, 397(1-2), 93-111. https://doi:10.1016/j.tecto.2004.10.005

Langhi, L., & Borel, G. D. (2008). Reverse structures in accommodation zone and early compartmentalization of extensional system, Laminaria High (NW shelf, Australia). Marine and Petroleum Geology, 25(8), 791-803. https://doi:10.1016/j.marpetgeo.2008.04.007

Langhi, L., Zhang, Y., Gartrell, A., Brincat, M. P., Lisk, M., Underschultz, J., & Dewhurst, D. (2013). 2. Mechanism of upfault seepage and seismic expression of hydrocarbon discharge sites from the

Timor Sea. Hydrocarbon Seepage: From Source to Surface. Society of Exploration Geophysicists and American Association of Petroleum Geologists, 11, 41. https://doi.org/10.1190/1.9781560803119.ch2

Lewis, M. M., Jackson, C. A. L., & Gawthorpe, R. L. (2013). Salt-influenced normal fault growth and forced folding: The Stavanger Fault System, North Sea. Journal of Structural Geology, 54, 156-173. https://doi.org/10.1016/j.jsg.2013.07.015

Long, J. J., & Imber, J. (2012). Strain compatibility and fault linkage in relay zones on normal faults. Journal of Structural Geology, 36, 16-26. https://doi.org/10.1016/j.jsg.2011.12.013

Naliboff, J., & Buiter, S. J. (2015). Rift reactivation and migration during multiphase extension. Earth and Planetary Science Letters, 421, 58-67.

Nixon, C. W., Sanderson, D. J., Dee, S. J., Bull, J. M., Humphreys, R. J., & Swanson, M. H. (2014). Fault interactions and reactivation within a normal-fault network at Milne Point, Alaska. AAPG Bulletin, 98(10), 2081-2107. http://dx.doi.org/10.1306/04301413177

O'Brien, G. W., Etheridge, M. A., Willcox, J. B., Morse, M., Symonds, P., Norman, C., & Needham, D. J. (1993). The structural architecture of the Timor Sea, north-western Australia: implications for basin development and hydrocarbon exploration. The APPEA Journal, 33(1), 258-279. https://doi.org/10.1071/AJ92019

Philippon, M., Willingshofer, E., Sokoutis, D., Corti, G., Sani, F., Bonini, M., & Cloetingh, S. (2015). Slip re-orientation in oblique rifts. Geology, 43(2), 147-150. https://doi.org/10.1130/G36208.1

Phillips, T. B., Jackson, C. A. L., Bell, R. E., & Duffy, O. B. (2018). Oblique reactivation of lithosphere-scale lineaments controls rift physiography–the upper-crustal expression of the Sorgenfrei–Tornquist Zone, offshore southern Norway. Solid Earth, 9(2), 403-429. https://doi.org/10.5194/se-9-403-2018

Phillips, T. B., Jackson, C. A. L., & Norcliffe, J. R. (2020). Pre-inversion normal fault geometry controls inversion style and magnitude, Farsund Basin, offshore southern Norway. Solid Earth, 11(4), 1489-1510. https://doi.org/10.5194/se-11-1489-2020

Reeve, M. T., Bell, R. E., Duffy, O. B., Jackson, C. A. L., & Sansom, E. (2015). The growth of non-colinear normal fault systems; What can we learn from 3D seismic reflection data?. Journal of Structural Geology, 70, 141-155.

Reilly, C., Nicol, A., & Walsh, J. (2017). Importance of pre-existing fault size for the evolution of an inverted fault system. Geological Society, London, Special Publications, 439(1), 447-463. https://doi.org/10.1144/SP439.2

Jackson, C. A. L., & Rotevatn, A. (2013). 3D seismic analysis of the structure and evolution of a salt-influenced normal fault zone: a test of competing fault growth models. Journal of Structural Geology, 54, 215-234. https://doi.org/10.1016/j.jsg.2013.06.012

Saqab, M. M., Bourget, J., Trotter, J., & Keep, M. (2017). New constraints on the timing of flexural deformation along the northern Australian margin: implications for arc-continent collision and the development of the Timor Trough. Tectonophysics, 696, 14-36. https://doi.org/10.1016/j.tecto.2016.12.020

Schöpfer, M. P., Childs, C., & Walsh, J. J. (2007). Two-dimensional distinct element modeling of the structure and growth of normal faults in multilayer sequences: 2. Impact of confining pressure and strength contrast on fault zone geometry and growth. Journal of Geophysical Research: Solid Earth, 112(B10). https://doi.org/10.1029/2006JB004903

de Ruig M. Trupp M.J., Bishop D.J. , Kuek D. Castillo D.A. (2000). Fault architecture and the mechanics of fault reactivation in the Nancar Trough/Laminaria area of the Timor Sea, Northern Australia. The APPEA Journal 40, 174-193.

Walsh, J. J., Childs, C., Meyer, V., Manzocchi, T., Imber, J., Nicol, A., ... & Strand, J. (2001). Geometric controls on the evolution of normal fault systems. Geological Society, London, Special Publications, 186(1), 157-170.

Walsh, J. J., Bailey, W. R., Childs, C., Nicol, A., & Bonson, C. G. (2003). Formation of segmented normal faults: a 3-D perspective. Journal of Structural Geology, 25(8), 1251-1262.

Whipp, P. S., Jackson, C. L., Gawthorpe, R. L., Dreyer, T., & Quinn, D. (2014). Normal fault array evolution above a reactivated rift fabric; a subsurface example from the northern Horda Platform, Norwegian North Sea. Basin Research, 26(4), 523-549.

Withjack, M. O., Henza, A. A., & Schlische, R. W. (2017). Three-dimensional fault geometries and interactions within experimental models of multiphase extension. AAPG Bulletin, 101(11), 1767-1789.

Yeates, A. N., Bradshaw, M. T., Dickins, J. M., Brakel, A. T., & Exon, N. F. (1987). The Westralian superbasin: an Australian link with Tethys. In International Symposium on Shallow Tethys 2 (pp. 199-213).

Zwaan, F., Chenin, P., Erratt, D., Manatschal, G., & Schreurs, G. (2021). Complex rift patterns, a result of interacting crustal and mantle weaknesses, or multiphase rifting? Insights from analogue models. Solid Earth Discussions, 1-38. https://doi.org/10.5194/se-2020-214